The effect of greenhouse gas–induced warming on the impact of El Niño and La Niña events on daily precipitation extremes in the boreal cold season

Qiaohong Sun, Francis W. Zwiers, Xuebin Zhang, & Yaheng Tan

2023

Pacific Climate Impacts Consortium (PCIC)

PCIC Publications

© 2023 American Meteorological Society. In compliance with funder open access policies, AMS makes all articles freely and publicly available one year from the date of final publication. https://www.ametsoc.org/ams/publications/ethical-guidelines-and-ams-policies/ams-licenses-for-journal-article-reuse/.

Original citation:

Sun, Q., Zwiers, F. W., Zhang, X., & Tan, Y. (2023). The effect of greenhouse gas–induced warming on the impact of El Niño and La Niña events on daily precipitation extremes in the boreal cold season. *Journal of Climate*, *36*(18), 6393–6407. https://doi.org/10.1175/JCLI-D-22-0713.1

Downloaded from UVicSpace Research & Learning Repository

dspace.library.uvic.ca

University of Victoria | Libraries

The Effect of Greenhouse Gas–Induced Warming on the Impact of El Niño and La Niña Events on Daily Precipitation Extremes in the Boreal Cold Season

QIAOHONG SUN,[a,b,c] FRANCIS ZWIERS,[b,d] XUEBIN ZHANG,[e] AND YAHENG TAN[f]

[a] *Key Laboratory of Meteorological Disaster of Ministry of Education, Joint International Research Laboratory of Climate and Environment Change, Nanjing University of Information Science and Technology, Nanjing, China*
[b] *Pacific Climate Impacts Consortium, University of Victoria, Victoria, British Columbia, Canada*
[c] *Collaborative Innovation Center on Forecast and Evaluation of Meteorological Disaster, Nanjing University of Information Science and Technology, Nanjing, China*
[d] *Nanjing University of Information Science and Technology, Nanjing, China*
[e] *Climate Research Division, Environment and Climate Change Canada, Toronto, Ontario, Canada*
[f] *Guizhou Climate Center, Guiyang, China*

(Manuscript received 16 September 2022, in final form 7 May 2023, accepted 1 June 2023)

ABSTRACT: El Niño–Southern Oscillation (ENSO) has a profound influence on the occurrence of extreme precipitation events at local and regional scales in the present-day climate, and thus it is important to understand how that influence may change under future global warming. We consider this question using the large-ensemble simulations of CESM2, which simulates ENSO well historically. CESM2 projects that the influence of ENSO on extreme precipitation will strengthen further under the SSP3–7.0 scenario in most regions whose extreme precipitation regimes are strongly affected by ENSO in the boreal cold season. Extreme precipitation in the boreal cold season that exceeds historical thresholds is projected to become more common throughout the ENSO cycle. The difference in the intensity of extreme precipitation events that occur under El Niño and La Niña conditions will increase, resulting in "more extreme and more variable hydroclimate extremes." We also consider the processes that affect the future intensity of extreme precipitation and how it varies with the ENSO cycle by partitioning changes into thermodynamic and dynamic components. The thermodynamic component, which reflects increases in atmospheric moisture content, results in a relatively uniform intensification of ENSO-driven extreme precipitation variation. In contrast, the dynamic component, which reflects changes in vertical motion, produces a strong regional difference in the response to forcing. In some regions, this component amplifies the thermodynamic-induced changes, while in others, it offsets them or even results in reduction in extreme precipitation variation.

KEYWORDS: ENSO; Extreme events; Ensembles

1. Introduction

Extreme precipitation can induce floods, landslides, soil erosion, damage to property and infrastructure, and even loss of life. El Niño–Southern Oscillation (ENSO), which is the most prominent global-scale mode of interannual variability, impacts many regions of the globe through atmospheric teleconnections, affecting extreme weather events worldwide. Previous studies suggest that ENSO influences different parts of the daily precipitation distribution differently, and that impacts on precipitation extremes could be particularly strong (Kenyon and Hegerl 2010). For example, over an extended part of North America, a daily precipitation event in the boreal cold season that occurs once every 20 La Niña years will occur between 2 and 4 times as often during El Niño years (Schubert et al. 2008; Zhang et al. 2010) and the probability of extremal precipitation occurring at multiple sites in the same season is also higher (Shang et al. 2011). Over South America, ENSO has shown to have significant influence on 3-day precipitation events that exceed the 90th percentile of such events (Grimm and Tedeschi 2009). ENSO also affects extreme precipitation in other parts of the world, including Indonesia (Supari et al. 2018; Kurniadi et al. 2021), the Arab region (Donat et al. 2014), Australia (King et al. 2013), and East Africa (Taylor et al. 2013).

The sixth assessment report of the Intergovernmental Panel on Climate Change (IPCC AR6) concluded that the future amplitude of ENSO rainfall variability will *very likely* intensify in response to global warming over the twenty-first century regardless of changes in ENSO sea surface temperature (SST) variability (Lee et al. 2021). Greenhouse warming intensifies ENSO-driven variability of boreal winter tropical upper-tropospheric temperature and geopotential height, tropical humidity, subtropical jets, and tropical Pacific rainfall (Hu et al. 2021). The associated ENSO precipitation variability on regional scales is therefore also likely to intensify (Power et al. 2013; Cai et al. 2015; Bonfils et al. 2015; Power and Delage 2018; Sun et al. 2020; Yang et al. 2021; Singh et al. 2022).

Most previous studies have, however, focused on the changes in the influence of ENSO on monthly or seasonal precipitation totals even though ENSO is often a predominant

Denotes content that is immediately available upon publication as open access.

Supplemental information related to this paper is available at the Journals Online website: https://doi.org/10.1175/JCLI-D-22-0713.s1.

Corresponding author: Qiaohong Sun, sunqh@nuist.edu.cn

DOI: 10.1175/JCLI-D-22-0713.1

© 2023 American Meteorological Society. This published article is licensed under the terms of the default AMS reuse license. For information regarding reuse of this content and general copyright information, consult the AMS Copyright Policy (www.ametsoc.org/PUBSReuseLicenses).

Brought to you by UNIVERSITY OF VICTORIA | Unauthenticated | Downloaded 03/18/25 10:15 PM UTC

factor in the occurrence of extreme precipitation events at local and regional scales (Zhang et al. 2010). Studies available to date have not considered whether projected climate changes will affect ENSO's influence on the most extreme types of daily precipitation events, and thus this article addresses that question.

Given that extreme weather often results from ENSO-induced anomalous atmospheric circulation, it is important to ask how ENSO-related extreme weather will change in the future. Warming will play an important role because the atmospheric water-holding capacity increases roughly exponentially with temperature, which influences the changes in the daily extreme precipitation intensity under warmer climates (Li et al. 2021; Sun et al. 2021). Extreme precipitation is influenced by both moisture and circulation (Huang and Xie 2015), and thus by ENSO. A moisture budget decomposition can help partition the ENSO-driven variation of extreme precipitation into dynamic and thermodynamic contributions. The recent advent of several large-ensemble climate simulations provides an opportunity to study these issues more closely because they provide large amounts of data that can be used to produce statistically robust estimates of changes in ENSO-related extreme weather, particularly for rare events. Here we aim to 1) quantify changes in ENSO-related extreme precipitation with different intensity in the future warmer climate with large ensembles, 2) characterize the changing risks of extreme precipitation conditional on different ENSO phases, and 3) understand the role of thermodynamic and dynamic effects on their changes.

This paper is structured as follows. Section 2 describes the observational data and model simulations used in this study, as well as the analysis methods. Climate model performance in reproducing ENSO characteristics and teleconnections with extreme precipitation is evaluated in section 3. The results of our analyses of future ENSO-related changes in extreme precipitation are provided in section 4, and their interpretation in view of physical mechanisms is discussed in section 5. Discussion and conclusions are given in sections 6 and 7.

2. Data and methods

a. Index definition and datasets

We identify ENSO events using an index based on smoothed monthly mean SST anomalies, similarly to Planton et al. (2021). SST anomalies are obtained by linearly detrending monthly mean SST, then calculating anomalies relative to the seasonal cycle of detrended SSTs, and finally smoothing the resulting anomalies with a 5-month triangular-weighted moving average filter. An ENSO index is obtained by spatially averaging the smoothed anomalies over the Niño-3.4 region (5°S–5°N, 120°–170°W). A year is classified as an El Niño year when the December value of the index exceeds 0.75 standard deviations (STD) and similarly identify La Niña events by the occurrence of index values that fall below −0.75 STD. We compared the results using 0.75, 1.0, and 1.5 STD as criteria to define ENSO events and found that the results were very similar. Therefore, we report only the results obtained using 0.75 STD as the criterion in this paper.

We use November–April (NDJFMA) maximum 1-day precipitation amounts (Rx1day) to represent extreme precipitation in the boreal cold season and examine the relationship of these extremes with ENSO variability. We consider seasonal maximum one-day precipitation amounts because of their relevance to local societal and economic impacts and because the magnitudes of rare events, such as those expected to recur once every 20 or 50 years on average, are frequently used in the design of infrastructure. In some areas, the November to April daily maximum precipitation as obtained from ERA5 can frequently be of a magnitude comparable to the levels that are usually classified as model drizzle (daily accumulations of less than 1 mm). To avoid analyzing such precipitation, we have masked out grid boxes for which more than 10% of years have November–April Rx1day below 1 mm during the evaluation period based on the ERA5. This should eliminate the inclusion of areas where spurious, out of season extremes are likely to occur in the observationally constrained reference data. The resulting mask is applied to both ERA5 and the model output.

We consider indices that are based on both observations and climate model simulations. We compute an observed ENSO index using the NOAA Extended Reconstructed Sea Surface Temperature dataset, version 5 (ERSSTv5; Huang et al. 2017). Annual observationally constrained NDJFMA Rx1day values are calculated using daily precipitation from reanalysis datasets, which, while not perfect, have complete spatial coverage. The reanalysis datasets considered are ERA5 (Hersbach et al. 2020), NCEP1 (Kalnay et al. 1996), JRA55 (Ebita et al. 2011), and MERRA (Rienecker et al. 2011). Although reanalysis data provide spatially and temporally complete data, they may contain biases and inhomogeneities caused by the use of models in reanalysis systems and variations in the quality, sources, and coverage of assimilated data. We therefore also use HadEX3, which is a gridded dataset of extremes indices derived from land-based station data (Dunn et al. 2020) for comparison with the reanalysis datasets. See section 2b for the selection of reanalysis datasets.

For the models, we consider three CMIP6 global models that have provided large initial conditions ensembles with simulations from 1850 to 2100 under historical (Eyring et al. 2016) and SSP3–7.0 (O'Neill et al. 2016) forcings, including 50 members from CanESM5, 50 members from CESM2, and 40 members from ACCESS-ESM-5. Large-ensemble climate simulations are used to examine simulated historical ENSO-related extreme precipitation and their projected changes in future climate under the SSP3–7.0 scenario. Given the complexity of climate models and the multiscale interactions that they simulate, it is essential to know which models simulate ENSO characteristics and teleconnections with extreme precipitation best before using them. We therefore first evaluate the performance of these models and then select the best performing of these models for assessing future projections and a detailed moisture budget decomposition.

Brought to you by UNIVERSITY OF VICTORIA | Unauthenticated | Downloaded 03/18/25 10:15 PM UTC

TABLE 1. ENSO metrics used in the study. ENSO metrics are calculated for the period 1979–2013.

ENSO metrics	Description	Unit
ENSO pattern	Equatorial Pacific sea surface temperature anomalies relative to the average during the 1981–2010 period: December Niño-3.4 SSTA regressed onto December SSTA across the Equatorial Pacific	°C °C^{-1}
ENSO amplitude	Standard deviation (S) of SST anomalies in the central equatorial Pacific (5°N–5°S, 170°–120°W). $S = \sqrt{\sum_{i=1}^{N}\lvert X_i - \overline{X}\rvert/(N-1)}$, where X_i is the Niño 3.4 SST anomaly in year i, $\overline{X}$ is the mean of X over all years, and N is the number of years.	°C
ENSO seasonality	ENSO seasonal timing: Ratio of the STD of Niño-3.4 SSTA in NDJ with that in MAM	—
ENSO cycle	Mean time between El Niño events	years
SST-Taux_feedback	Ocean–atmospheric Bjerknes feedback; computed by regressing zonal wind stress anomalies relative to the average during the 1981–2010 period (TauxA) in the western equatorial Pacific [horizontal Niño-4 (5°N–5°S, 160°E–150°W) average] onto sea surface temperature anomalies (SSTAs) in the eastern equatorial Pacific [horizontal Niño-3 (5°N–5°S, 150°–90°W) average]	N m^{-2} °C^{-1}
Rx1day_tc	ENSO-Rx1day teleconnection pattern over global land during November–April (based on regression)	mm °C^{-1}

b. *Reference data for model evaluation*

Following Planton et al. (2021), we use six ENSO evaluation metrics to evaluate model performance in simulating ENSO, including ENSO pattern, ENSO amplitude, ENSO seasonality, the length of the ENSO cycle, the strength of the ocean–atmosphere Bjerknes feedback (SST-Taux_feedback), and the structure of ENSO winter extreme precipitation teleconnection patterns (Rx1day_tc). Details of these metrics are provided in Table 1. Specifically, as the Walker circulation's strength influences ENSO-driven teleconnections (e.g., Klein et al. 1999), we used the SST-Taux_feedback to estimate the impact of that process. Additionally, we used Rx1day_tc, which we defined as the linear regression of extreme precipitation during boreal cold season onto the ENSO index, to describe the teleconnection relationship between precipitation extremes and ENSO.

We compute the observed ENSO pattern, ENSO amplitude, ENSO seasonality, and ENSO cycle length during 1950–2013 using ERSSTv5, which is regarded as the reference to evaluate the performance of models' simulations.

Rx1day_tc patterns are evaluated based on reanalysis data because of lack of full spatial coverage by HadEX3. The evaluation is conducted using the period 1979–2013 because all reanalysis datasets cover the period beginning from 1979, after which reanalysis products have markedly higher quality than during the presatellite period (Uppala 2007), and because models with historical forcing end in 2014. Rx1day_tc patterns are calculated using precipitation data from a reanalysis dataset that has an ENSO-Rx1day teleconnection pattern closest to that of the HadEX3 precipitation over the areas where HadEX3 has sufficient coverage for the period 1979–2013. To select the best reanalysis dataset as the reference dataset for model evaluation, we obtained the teleconnection patterns for the period 1979–2013 using HadEX3 precipitation and different reanalysis datasets over the grids where HadEX3 provides coverage. Then, we use Taylor diagram to compare the teleconnection patterns derived from the reanalysis datasets with that from the HadEX3 (Fig. S1 in the online supplemental material). Based on this evaluation, we select ERA5 as the reference dataset for model evaluation as it performed the best among reanalyses with higher spatial correlation and lower biases for the teleconnection patterns.

Monthly zonal wind stress from ERA5 for the period 1979–2013 is also used to calculate the metric of the ocean–atmosphere Bjerknes feedback (SST-Taux_feedback) as the reference for model evaluation.

All data from the selected reanalysis and the CanESM5, CESM2, and ACCESS-ESM-5 large-ensemble simulations are interpolated onto a 1° latitude × 1° longitude grid prior to index calculation, comparison, and model evaluation.

c. *ENSO-driven extreme precipitation variation*

A concept we use extensively in this paper is that of *ENSO-driven extreme precipitation variation*, which refers to the difference in extreme precipitation that occurs between El Niño and La Niña conditions in historical (1950–99) and future (2050–99) periods. Here we use the framework similar to that introduced by Power and Delage (2018) in their examination of forced changes in ENSO-driven seasonal average precipitation variation. We also use the concepts of El Niño–driven deviation and La Niña–driven deviation to refer to the differences in extreme precipitation during El Niño or La Niña phases and neutral phase.

To quantify changes in ENSO-driven extreme precipitation variation of different intensities in the future warmer climate with large ensembles, we compare percentiles of model simulated NDJFMA Rx1day values during different ENSO phases in historical (1950–99) and future (2050–99) periods.

In historical period, to consider the rarity of extreme precipitation, we first estimate the 50th, 95th, and 98th percentiles of historical period NDJFMA Rx1day during model simulated El Niño, neutral, and La Niña years as empirical estimates of the magnitude of model simulated 2-, 20-, and 50-yr extreme NDJFMA Rx1day events under those different ENSO conditions. These estimated return levels are denoted $E_{h,x}$ (El Niño), $N_{h,x}$ (neutral), and $L_{h,x}$ (La Niña), respectively, where subscript h

Brought to you by UNIVERSITY OF VICTORIA | Unauthenticated | Downloaded 03/18/25 10:15 PM UTC

refers to the historical period and x refers to the return period (2, 20, or 50 years). The effect of El Niño and La Niña on extreme precipitation relative to neutral conditions is estimated as El Niño–driven deviation ($\delta E_{h,x} = E_{h,x} - N_{h,x}$) and La Niña–driven deviation ($\delta L_{h,x} = L_{h,x} - N_{h,x}$), respectively. Also, we use $V_{h,x} = \delta E_{h,x} - \delta L_{h,x} = E_{h,x} - L_{h,x}$ (i.e., the difference between extreme precipitation in El Niño and La Niña years) as a measure of ENSO-driven extreme precipitation variation.

Analogous return levels ($E_{f,x}$, $N_{f,x}$, and $L_{f,x}$) and diagnostics are calculated from the future period, which is designated by the subscript f. Changes in these statistics between historical and future periods, which are calculated as $\Delta\delta E_x = \delta E_{f,x} - \delta E_{h,x}$, $\Delta\delta L_x = \delta L_{f,x} - \delta L_{h,x}$, and $\Delta V_x = V_{f,x} - V_{h,x}$, are used to see if El Niño–, La Niña–, and ENSO-driven variation of extreme precipitation in the future climate state will change relative to the historical period. The choice of the length of the historical and future periods represents a trade-off. As the period for calculating ENSO statistics lengthens, the influence of internal variability tapers off making it easier to evaluate the effect of greenhouse-induced warming. On the other hand, nonstationarity will more strongly affect the representativeness of percentile estimates during long periods of transient response to external forcing than during shorter periods. To the extent that the responses to forcing over the analysis periods are roughly linear, differences between relatively long historical and future periods can be considered as being representative of the change between the midpoints of these periods. Since the questions of interest pertain to extremes, which are inherently noisy, we have prioritized the reduction of the influence of internal variability that is afforded by using relatively long 50-yr historical and future periods.

d. Probability analysis

A benefit of using a large ensemble is that more confident return period estimates can be made for large events. The combination of relatively long analysis periods together with the availability of many ensemble members means that for a model with 50-ensemble members, a sample of 2500 annual index values are available for each analysis period (2000 in the case of the ACCESS-ESM-5 large ensemble, which has 40 rather than 50 members). These large samples provide sufficient realizations in each of the different ENSO phases to estimate the probability of the occurrence of high-impact extreme precipitation event under those conditions with confidence, both under historical and future climate states.

We perform three kinds of comparisons to characterize the changing risks of extreme precipitation conditional on different ENSO phases and how those risks may change in the future. First, we consider the effects of ENSO and future warming on extreme precipitation events that are defined based on historical neutral phase conditions, considering 2-, 20-, and 50-yr events. For the historical period, we estimate the probability of neutral phase events of magnitude $N_{h,x}$ during historical El Niño and La Niña phases, and this probability is then divided by the corresponding nominal neutral phase probability of 0.5, 0.05, or 0.02, respectively. These "risk ratios" provide estimates of the relative risk of occurrence of $N_{h,x}$ events during different ENSO phases under historical forcing conditions.

Second, we also ask if the impact of ENSO in the future relative to future neutral conditions is different from its impact in the historical climate relative to historical neutral conditions as simulated by the climate models. To do so, we use future neutral phases as the reference period and $N_{f,x}$ as the reference event values, and then again estimate risk ratios under future El Niño and La Niña phases.

Third, we calculate risk ratio for future El Niño, neutral, and La Niña by using historical El Niño ($E_{h,x}$), neutral ($N_{h,x}$), and La Niña ($L_{h,x}$) year events as the reference event values, respectively. This allows us to obtain risk ratios for future events that are directly comparable with historical period events to see if the frequencies of extreme precipitation under different ENSO phases change relative to their historical frequencies with warming.

e. Moist budget decomposition of changes in ENSO-driven extreme precipitation variation

To understand the effects of thermodynamic and dynamic changes on changes in ENSO-driven extreme precipitation variation, we apply the moisture budget decomposition suggested in Huang and Xie (2015) to partition the ENSO-driven variability of extreme precipitation in the large-ensemble simulations into dynamic and thermodynamic contributions. Here we consider changes in surface specific humidity (q) to be of thermodynamic origin and consider the changes in ENSO-driven vertical motion variation as indicated by 500-hPa vertical velocity (w) as the dynamic component. First, we extracted daily w and q values corresponding to the time and location of occurrence of DJF Rx1day events. Second, similar to the calculation steps in section 2c, we estimate the 50th, 95th, and 98th percentiles of these extracted w and q values during model simulated El Niño, neutral, and La Niña years as empirical estimates of moisture and circulation conditions for the 2-, 20-, and 50-yr extreme NDJFMA Rx1day events under El Niño, neutral and La Niña conditions as well as during historical and future periods; then we calculate the corresponding $\delta w_{h,x}$, $\delta q_{h,x}$, $\Delta\delta w_x$, and $\Delta\delta q_x$ [where x refers to the length of the return period (2, 20, or 50 years) as in section 2c] as the measure of ENSO-driven surface specific humidity and vertical motion variation as well as their changes in future period relative to the historical period. Thus, the change in the ENSO-driven extreme precipitation variation (ΔV_x) can be decomposed as follows:

$$\Delta V_x \sim -(\Delta q_x \times \delta w_{h,x} + q_x \times \Delta\delta w_{h,x} + \Delta w_x \times \delta q_{h,x} + w_x \times \Delta\delta q_{h,x})/g. \quad (1)$$

In this expression, q_x and w_x are, respectively, the unconditional specific humidity and 500-hPa vertical velocity mean states, that is, all data samples are used to estimate the 50th, 95th, and 98th percentiles of these extracted w and q values. As mentioned above, $\delta w_{h,x}$ and $\delta q_{h,x}$ are their historical ENSO-driven variations, and g is the acceleration due to gravity. This decomposition partitions ΔV into three components:

Brought to you by UNIVERSITY OF VICTORIA | Unauthenticated | Downloaded 03/18/25 10:15 PM UTC

a thermodynamic component $-\Delta q_x \times \delta w_{h,x}$ that it is due to changes in background moisture field, a dynamic component $-q_x \times \delta w_{h,x}$ due to change in the ENSO-driven vertical motion variation, and a covariation term $-(\Delta w_x \times \delta q_{h,x} + w_x \times \Delta\delta q_{h,x})$ that is negligible relative to the other two terms. We estimated the 50th, 95th, and 98th percentiles of these values during model simulated El Niño, neutral, and La Niña years as empirical estimates of circulation conditions for the 2-, 20-, and 50-yr extreme DJF Rx1day events under El Niño, neutral and La Niña conditions. We calculate this decomposition for three different return periods (2, 20, and 50 years) at each individual grid box. The grid box values are summarized at the regional scale for each region of interest by averaging across grid boxes in the region.

f. *Bootstrapping approach*

We quantify uncertainty ranges of the projected changes in ENSO-driven precipitation variation, risk ratio, and moisture and circulation changes by using a bootstrapping approach. For example, in the case of the changes in ENSO-driven extreme precipitation variation, we proceed by 1) randomly sampling with replacement El Niño (or La Niña) events from the set of historical/future El Niño (or La Niña) years, always retaining the same number of historical/future El Niño (or La Niña) years; 2) estimating the magnitude of model simulated 2-, 20-, and 50-yr extreme Rx1day events from the new sample, and calculating the difference between historical and future ENSO-driven extreme precipitation variation of different intensities; 3) repeating the first two steps 1000 times, and 4) finally estimating the 2.5th and 97.5th percentiles of the difference between historical and future ENSO-driven extreme precipitation variation for each return period from the 1000 bootstrap estimates to obtain an estimated 95% uncertainty range, which is used to determine if the changes in ENSO-driven extreme precipitation variation are significantly different from zero at the 5% significance level. The uncertainties of the risk ratios for probability analysis as well as moisture and circulation changes for the moist budget decomposition are estimated similarly.

3. Model selection

Figure 1 shows results evaluating the simulation of ENSO pattern, ENSO amplitude, seasonality, and cycle length using 1950–2013 as the evaluation period. Figure 1 shows that CESM2 performs better than other two models in reproducing the observed spatial structure of SSTA in the equatorial Pacific with higher correlation with observations and having the closer standard deviation as the observed (Figs. 1b,e). As observed, maximum SSTA values occur in the Niño-3.4 region in CESM2, while they are found too far east in CanESM5 and ACCESS-ESM1-5 (Figs. 1c,d). CESM2 substantially overestimates ENSO amplitude as indicated by Niño-3.4 SSTA (Fig. 1f). In contrast, ACCESS-ESM-5 and CanESM5 marginally underestimate ENSO amplitude (Fig. 1f). All models show weaker seasonality than observed, indicating that ENSO may occur too frequently during spring in the models. CESM2 performs somewhat better than the other two models in this regard (Fig. 1g). All models simulate ENSO events less frequently than observed. The mean time between El Niño events in CESM2 is marginally closer to observed than the other models. The large ensembles demonstrate that the natural variation in the length of the ENSO cycle is large in the models (Fig. 1h), suggesting that the observed value may also have been strongly affected by internal variability.

Figure 2 displays an evaluation of the simulation of SST-Taux_feedback and Rx1day_tc, but using 1979–2013 as the evaluation period, which is dictated by the period during which the reference reanalysis dataset is judged to be of highest quality and the 2014 end of the historical simulations in models. All models substantially underestimate the observed SST-to-Taux coupling strength. CESM2 performs slightly better than the other models, with about 55% of the observed SST-to-Taux coupling strength. For all three models, the difference between the observed and simulated coupling strengths would appear to be substantially larger than can be explained by internal variability, at least as simulated by the models. CESM2 again performs slightly better than the other models in Rx1day_tc, with a pattern correlation between the ERA5 and CESM2 teleconnection patterns of about 0.85 (versus ~0.7 for other models), and the spatial variance of the CESM2 pattern is about 75% of that in ERA5 (versus ~80% for CanESM5 and 50% for ACCESS-ESM-5). CESM2 can basically capture the spatial pattern of climatology and standard deviation of NDJFMA Rx1day during the 1979–2013 with 0.89 and 0.83 spatial correlation coefficients, respectively (Fig. S2).

Based on this brief evaluation of ENSO simulation performance, we selected CESM2 for further analysis. We made this choice because it performs better than other models in most ENSO metrics, even though it simulates substantially stronger than observed ENSO amplitude, and because it provides daily resolution data for all variables used in the moisture budget decomposition. In addition, to investigate the global spatial patterns of changes in ENSO related precipitation extremes, we also consider regional difference in the response to forcing and their physical mechanisms according to the moisture budget decomposition. We selected regions from the Iturbide et al. (2020) reference land regions, which were used by IPCC AR6 because they were felt to better represent regional climate features. We first identified regions for which there is a statistically significant correlation ($p < 0.05$) between the time series of the regional average NDJFMA Rx1day values and the ENSO index during the period 1979–2013 based on the ERA5. We then selected regions in which more than 45 members of the CEMS2 large ensemble correctly capture observed signals, and spatial patterns of the model and ERA5 are significantly correlated (Fig. 3). In the end, 11 regions were selected for analysis (Fig. 3), including eastern North America (ENA), northern Central America (NCA), southeastern South America (SESA), Southeast Asia (SEA), western central Asia (WCA), southern Australia (SAU), central Africa (CA), northern East Africa (NEAF), southern East Africa (SEAF), equatorial Pacific Ocean (EPO), and South Pacific Ocean (SPO).

Brought to you by UNIVERSITY OF VICTORIA | Unauthenticated | Downloaded 03/18/25 10:15 PM UTC

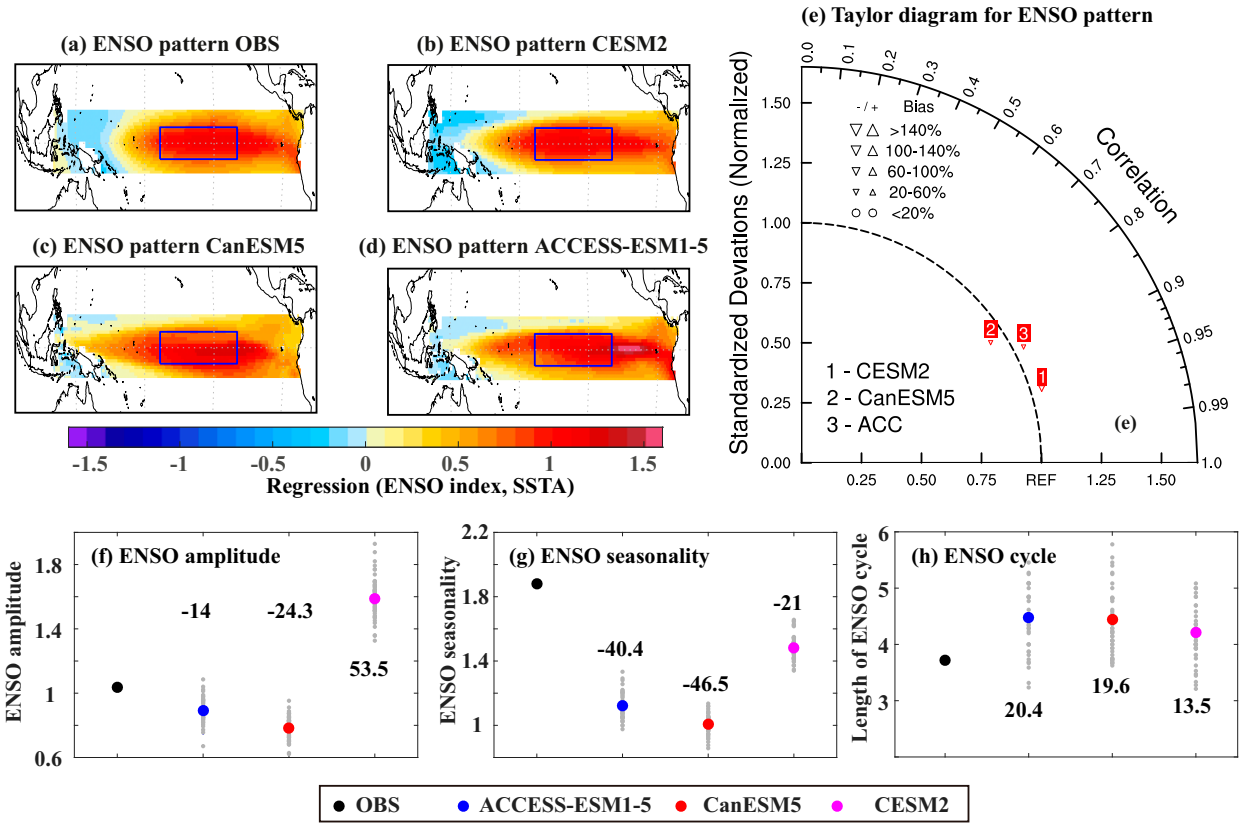

FIG. 1. Comparison of four ENSO metrics between the observational data and the three large-ensemble simulations based on the period 1950–2013. (a)–(d) The spatial patterns of sea surface temperature anomalies (SSTA) associated with ENSO index in the equatorial Pacific for the reference and the models (CESM2, ACCESS-ESM1-5, and CanESM5), respectively. (e) Taylor diagram comparing spatial patterns of SSTA associated with ENSO index from models with that from the references (ERSSTv5 for SSTA, ERA5 for Rx1day). (f)–(h) Evaluation results for ENSO amplitude, ENSO seasonality, and ENSO cycle, respectively. We pool data from all members to obtain the best estimate of the corresponding model. In (f)–(h), the blue, red, and magenta dots are best estimates for ACCESS-ESM1-5, CanESM5, and CESM2, respectively; The gray dots indicate metrics calculated from individual ensemble members, the black numbers indicate the relative differences [100 × (model − observation)/observation] between the observation and the best estimates of model simulations.

4. Projected changes in ENSO related precipitation extremes

a. *Future spatial structure of extreme precipitation under different ENSO phases*

Figure 4 shows the global spatial patterns of El Niño–driven deviation, La Niña–driven deviation, and ENSO-driven variation of 20-yr NDJFMA maximum precipitation events in historical (1950–99) and future (2050–99) periods as well as their differences ($\Delta\delta E_{20}$, $\Delta\delta L_{20}$, ΔV_{20}) in the CESM2 large ensemble. Similar results for the 2- and 50-yr events are shown in supplemental (Figs. S3 and S4). In the future warmer climate state, the spatial patterns of El Niño–driven deviation, La Niña–driven deviation, and ENSO-driven extreme precipitation variation will remain broadly similar with historical climates over most regions with a few exceptions for all intensities of extreme precipitation (2-, 20-, and 50-yr events) considered (Fig. 4, Figs. S3 and S4). For instance, the amplitudes of 20-yr NDJFMA precipitation events tend to be larger in El Niño years relative to that in neutral years over the central and eastern Pacific Ocean, southeastern South America, Central Asia, the Arabian Peninsula, and northeastern Africa (Fig. 3d). This can be also seen in Figs. S5 and S6, which compare the estimated likelihood of an extreme precipitation event that is at least as large as historical or future neutral state 20- or 50-yr return values (i.e., events that recur once every 20 or 50 historical or future neutral years on average) conditional on the occurrence of El Niño and La Niña events. Compared with the neutral state, the risk ratio is larger than unity during El Niño years, meaning that extreme neutral year precipitation events are more likely to occur during El Niño years in these regions. In contrast, in the western Pacific Ocean, the Canadian prairies, northeastern South America, and Australia, extremes tend to be more intense and occur more frequently under La Niña conditions (Figs. S5 and S6).

The spatial patterns of the response of 2- and 50-yr extreme precipitation events to ENSO are broadly similar to those seen in 20-yr events in most affected areas, while the magnitudes of El Niño–driven deviation, La Niña–driven deviation, and ENSO-driven extreme precipitation variation and the risk ratio for more

Brought to you by UNIVERSITY OF VICTORIA | Unauthenticated | Downloaded 03/18/25 10:15 PM UTC

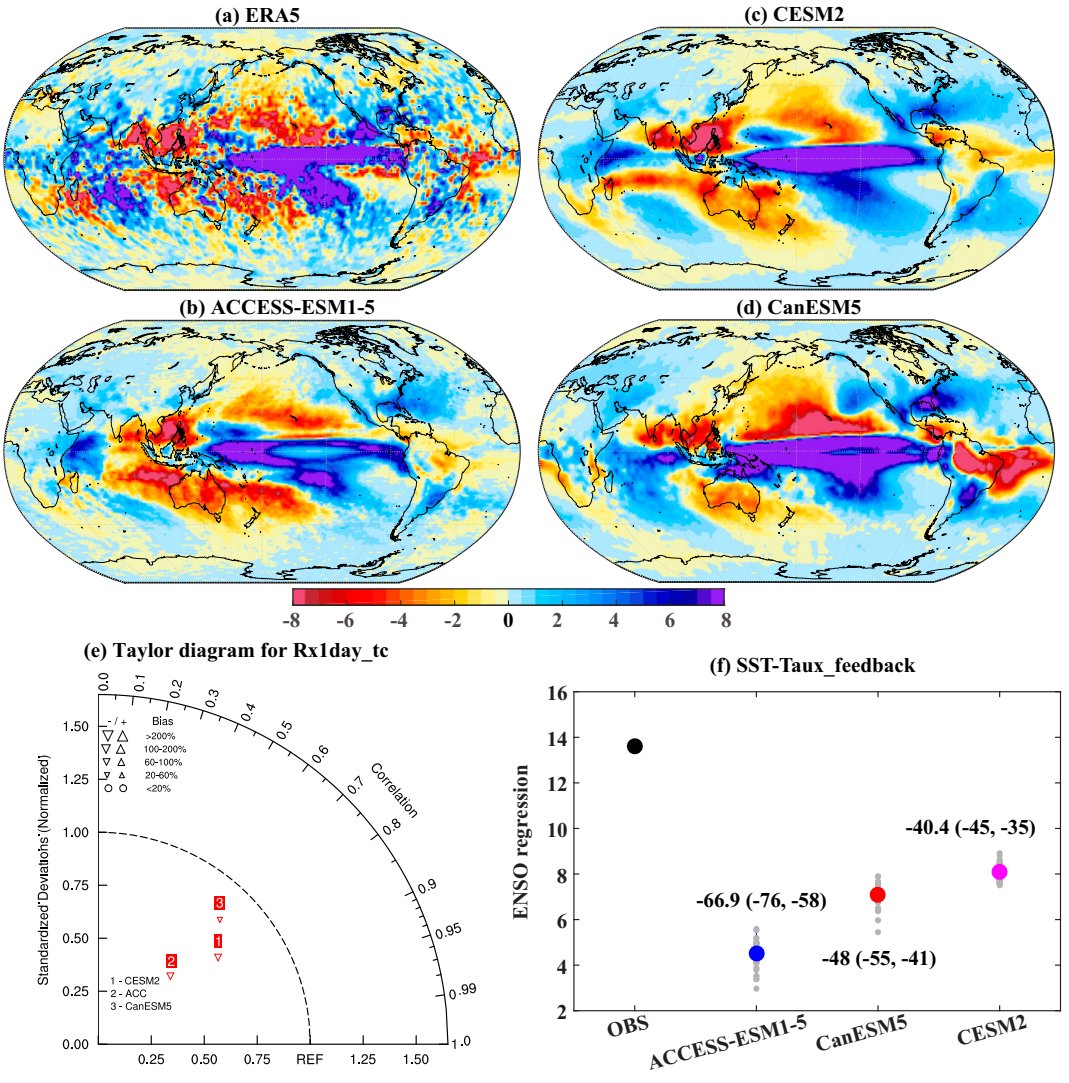

FIG. 2. Comparison of the spatial patterns of ENSO and DJF Rx1day teleconnection relationships and evaluation results for SST-Taux_feedback for the period 1979–2013 based on ERA5 and three CMIP6 global models providing large-ensemble simulations. (a)–(d) ENSO-driven extreme precipitation variation patterns in ERA5, CESM2, ACCESS-ESM1-5, and CanESM5, respectively. (e) Taylor diagram comparing Rx1day_tc spatial patterns from models with that from ERA5. (f) Evaluation results for SST-Taux_feedback based on the period 1979–2013, in which calculation processes are as in Figs. 1f and 1g.

extreme events are larger than those for less extreme events (Figs. S4–S6), indicating that the sensitivity to ENSO depends on the rarity of the extreme precipitation event. Consistent with findings reported previously concerning the response of precipitation extremes to external forcing in CMIP6 models (e.g., Li et al. 2021), ENSO responses in rarer events also tend to be larger.

b. *Future strength of ENSO-driven precipitation extremes and its variation*

The variance of the ENSO index does not increase in the future warmer climate, although there is a modest increase in the number of El Niño and La Niña events (Fig. S7). Nevertheless, results show two main changes in ENSO related precipitation extremes. First, El Niño– and La Niña–driven extreme precipitation deviations are projected to strengthen over most regions along with the corresponding ENSO-driven extreme precipitation variation (Figs. 4g–i). For example, positive El Niño–driven deviations and negative La Niña–driven deviations in 20-yr events are projected to increase in most locations over the equatorial Pacific Ocean, eastern North America, southeastern South America, western central Asia, and northern East Africa, which results in an increase in the ENSO-driven extreme precipitation variation (Fig. 4i). Therefore, the difference of extreme precipitation between El Niño and La Niña will increase with warming in these regions.

On the other hand, extreme precipitation under all ENSO phases will intensify in the future in most areas, which is a consequence of the warming-induced increase in tropospheric

Brought to you by UNIVERSITY OF VICTORIA | Unauthenticated | Downloaded 03/18/25 10:15 PM UTC

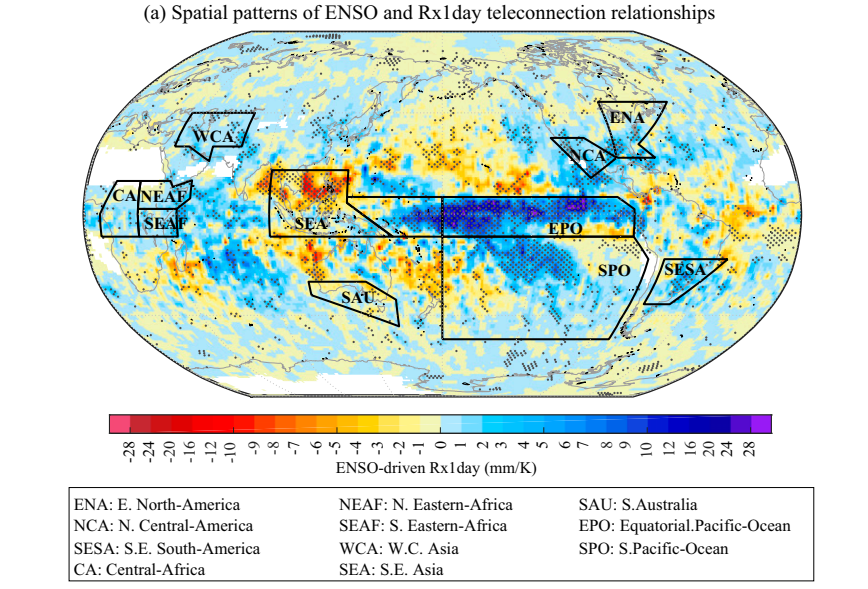

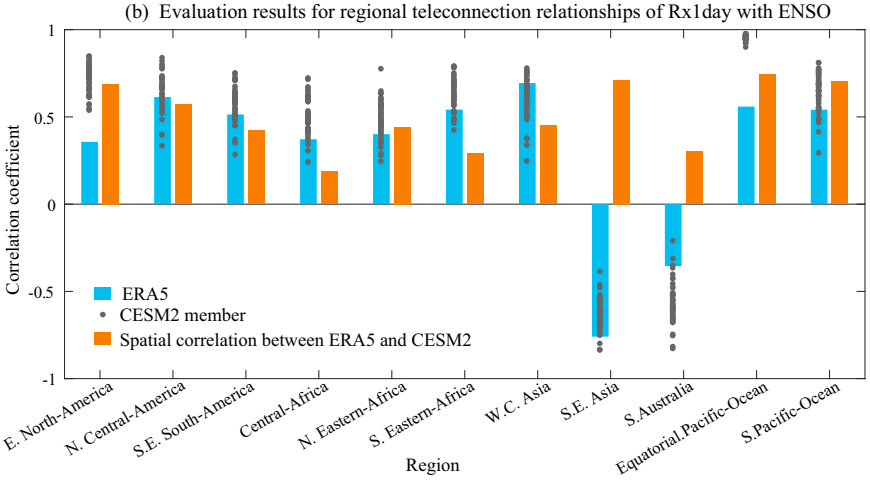

FIG. 3. (a) Correlation coefficient between the ENSO index and NDJFMA Rx1day during 1979–2014 period based on the ERA5 and (b) regional teleconnection over 11 selected regions and the performance of CESM2. Blue bars and gray dots indicate correlation coefficients between the time series of the regional average Rx1day and the ENSO index during the period 1979–2013 based on the ERA5 and each member of CESM2, respectively; orange bars indicate the spatial correlation coefficient of Rx1day_tc over each region. Dots in (a) indicate locations where the correlation relationship between the ENSO index and DJF Rx1day is statistically significant at the 10% level.

water vapor content. Compared to the historical period, the likelihood of extreme precipitation experienced under historical neutral, El Niño, and La Niño conditions is projected to increase in the future conditions in most regions. For instance, events with the intensity of historical El Niño 20-yr events are projected to occur more than 3.0 times as often in future El Niño years in most land areas (i.e., with risk ratios greater than 3.0 for 20-yr events; Fig. 5b). Similar results can be found in future neutral and La Niña phases relative to historical neutral and La Niña phases, respectively. Moreover, the spatial patterns of change in ENSO-driven extreme precipitation variation and risk ratios for 50-yr events are similar to those of 20-yr events in most affected regions, with greater intensification for rarer events (Figs. 5d–f).

It should be noted that there are exceptions in the southern subtropical regions around Mexico, where reductions in mean intensity of precipitation extremes in El Niño– and La Niña–driven deviations as well as the ENSO-driven extreme precipitation variability are projected.

Overall, changes in ENSO-driven NDJFMA extreme precipitation variation and the risk of the occurrence of extreme precipitation events in the future climate depend on locations. In

Brought to you by UNIVERSITY OF VICTORIA | Unauthenticated | Downloaded 03/18/25 10:15 PM UTC

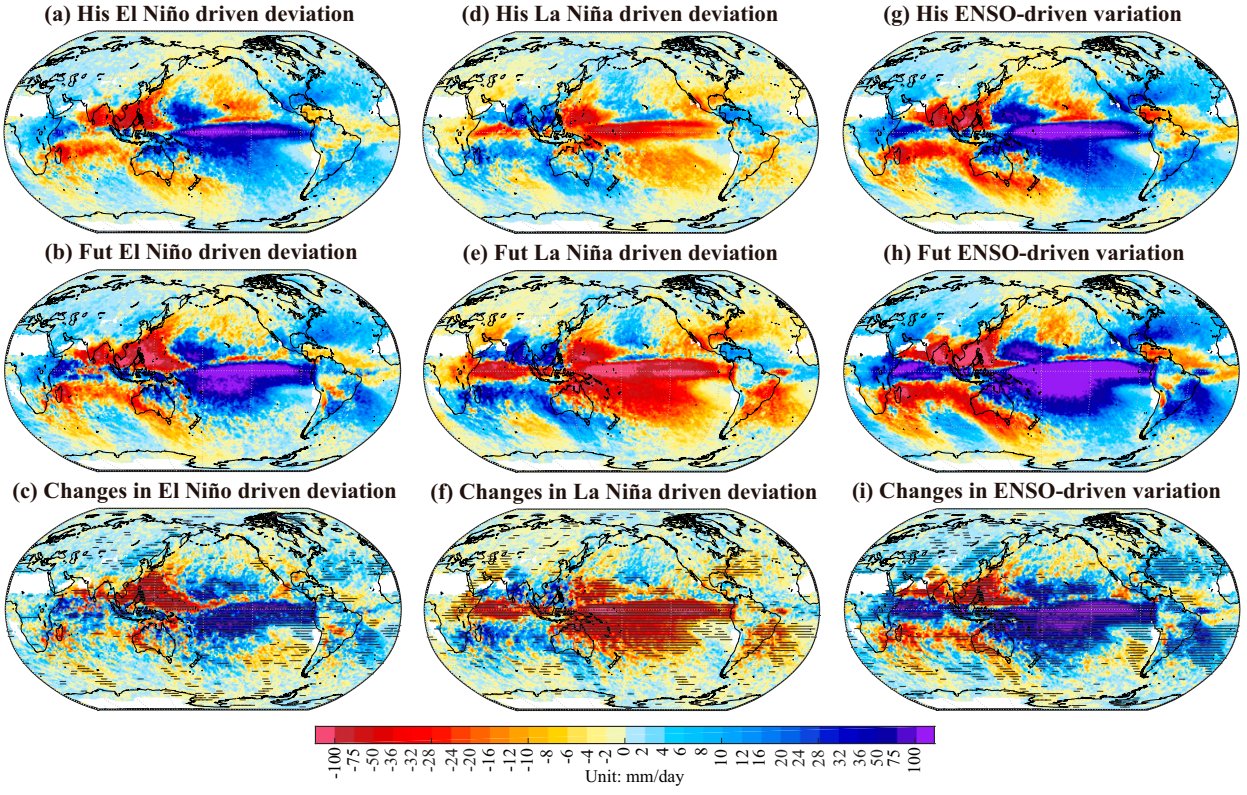

FIG. 4. Spatial patterns of El Niño–driven deviation, La Niña–driven deviation, and ENSO-driven variability of 20-yr NDJFMA maximum precipitation events in historical (His; 1950–99) and future (Fut; 2050–99) periods as well as their differences in the CESM2 large ensemble: (a),(d),(g) El Niño–driven deviation $\delta E_{h,20}$, $\delta E_{f,20}$, and $\Delta\delta E_{20}$, respectively; (b),(e),(h) La Niña–driven deviation $\delta L_{h,20}$, $\delta L_{f,20}$, and $\Delta\delta L_{20}$, respectively; and (c),(f),(i) for ENSO-driven extreme precipitation variation $V_{h,20}$, $V_{f,20}$, and ΔV_{20}, respectively. Hatching in (c), (f), and (i) indicates changes that are significantly different from zero at the 5% level.

most regions, such as the equatorial Pacific Ocean, eastern North America, southeastern South America, western central Asia, and northern East Africa, there would be an intensification of extreme precipitation in all ENSO phases, and the difference in extreme precipitation corresponding to El Niño and that to La Niña will increase with warming, resulting in "more extreme and more variable hydroclimate extremes." However, somewhat different behavior is seen in Central North America. The disparity of extreme precipitation between El Niño and La Niña in future is projected to decrease (Fig. 5c).

5. The role of thermodynamic and dynamical component

ENSO-driven extreme precipitation variation will be affected by changes in both the background moisture field and ENSO circulation in the future warmer climate. From the statistical perspective, if the projected change in extreme precipitation corresponds to simply scaling by a constant, then the change in ENSO-driven variation would be equal to the mean change in extreme precipitation unconditional on ENSO (Rind et al. 1989; Pendergrass et al. 2017). Also, if the precipitation rate depends linearly on near-surface moisture and moisture increase with no corresponding change in circulation, then we would expect that the change in extreme precipitation variation would equal the rate of moistening, on the order of 6%–7% $°C^{-1}$ of warming (Pendergrass et al. 2017).

Figure 6a shows regional averages of percentage changes per degree Celsius of warming in future ENSO-driven extreme precipitation variation relative to the period 1950–99 at the eleven selected regions. Similar to changes in extreme precipitation (Li et al. 2019; Pfahl et al. 2017), relative changes in ENSO-driven extreme precipitation variation with global warming show strong regional difference in response to global warming. Figures 6c and 6d shows regional averages of the contribution of thermodynamic and dynamic components, in which each component is also normalized by the historical ENSO-driven extreme precipitation variation and expressed in percent per degree Celsius global mean temperature change. The thermodynamic component contributes to a relatively uniform increase in extreme precipitation across most regions as well as all precipitation events. The thermodynamic effect intensifies ENSO-driven extreme precipitation variation by about 4%–9% $°C^{-1}$ across most regions and precipitation events with narrow uncertainty ranges (Fig. 6c), which is close to the change that might be expected from the Clausius–Clapeyron (CC) relationship. This is supported by Fig. S8, which shows that increases in specific humidity in the ENSO-neutral state and the

Brought to you by UNIVERSITY OF VICTORIA | Unauthenticated | Downloaded 03/18/25 10:15 PM UTC

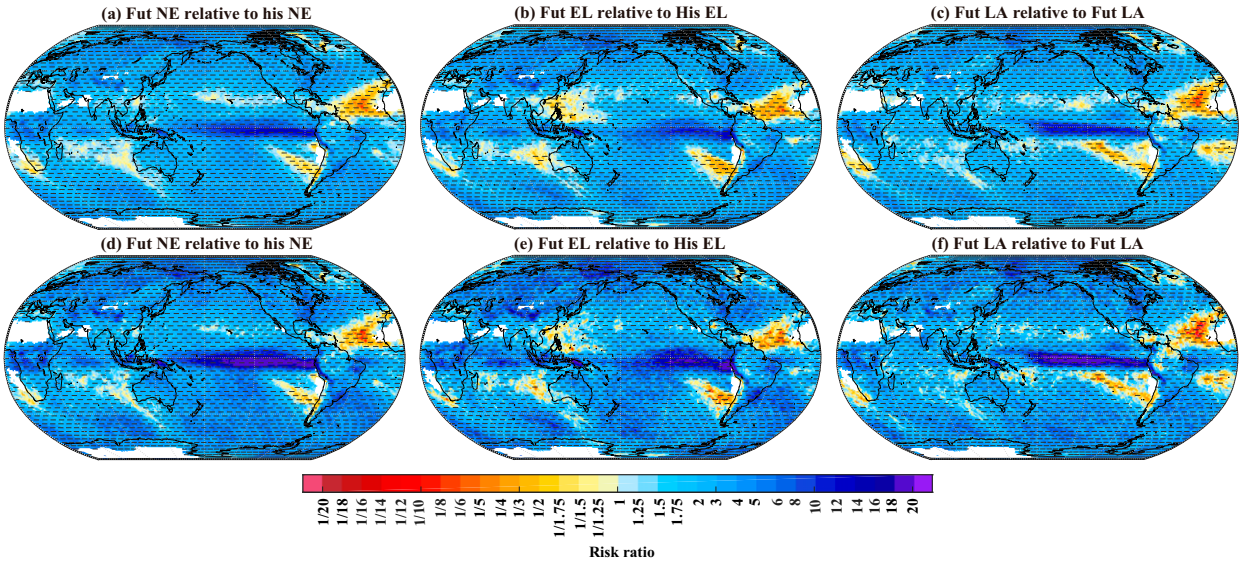

FIG. 5. Relative frequency changes (expressed as risk ratio) of extreme precipitation event that is at least as large as (a)–(c) 20- or (d)–(f) 50-yr return values during historical periods under future ENSO conditions. Frequency changes of extreme precipitation event for (a),(d) future neutral years with $N_{h,x}$ as the reference value; (b),(e) future El Niño years with historical El Niño ($E_{h,x}$) as the reference value; and (c),(f) future La Niña with historical La Niña ($L_{h,x}$) as the reference value. Hatching in (d)–(f) indicates values of risk ratio that are significantly different from unity at the 5% level.

unconditional state are spatially homogeneous for all intensities of extreme precipitation considered. These results illustrate that the thermodynamic response to greenhouse gas forcing amplifies the ENSO-driven extreme precipitation variation in most regions, by increasing total precipitable water.

Nevertheless, the thermodynamic component alone (Fig. 6c) does a poor job of describing the total change in the ENSO-driven extreme precipitation variation (Figs. 6a,b). The dynamic component produces strong regional difference in the response to forcing (Fig. 6d). It intensifies precipitation in some regions while reduces precipitation in other regions. As a result, the moisture-driven intensification is amplified or reduced. In the ENA, SESA, WCA, SAU, EPO, and SPO, the dynamic amplifies the thermodynamic-induced intensification of ENSO-driven extreme precipitation variation for all extreme precipitation intensities, with total component scaling higher than the thermodynamic component scaling (Fig. 6b). However, the dynamic component cancels out the influence of the mean-state moisture increases in the SEA and NCA. The total component scaling is smaller than the thermodynamic component scaling for all extreme precipitation intensities in NCA and for 2- and 50-yr events in SEA (Fig. 6b). Moreover, uncertainty ranges of dynamic component are larger than thermodynamic component.

Figure 7 shows the spatial patterns of the thermodynamic and dynamic contributions to changes in ENSO-driven extreme precipitation variation in units of mm day^{-1} to allow direct comparison with Fig. 4. The sum of the thermodynamic and dynamic components (Figs. 7a,d,g) accurately describes the global spatial patterns of changes in ENSO-driven extreme precipitation variation (Fig. 4i, Figs. S3i and S4i), with spatial correlation coefficients of 0.93, 0.97, and 0.96 for 2-, 20-, and 50-yr events, respectively. Therefore, the moisture budget decomposition which has been used previously to explain changes in ENSO-induced tropical Pacific mean rainfall variation (Huang and Xie 2015) can also be applied to ENSO-induced extreme precipitation variation outside the tropical strip. These spatial patterns confirm the above finding that the thermodynamic component alone would lead to a spatially homogeneous fractional increase in ENSO-driven extreme precipitation variation with percentage changes in response to global warming that are close to CC relation in most locations. Nevertheless, the final spatial patterns of change in ENSO-driven extreme precipitation variation (Fig. 4i) are strongly associated with the dynamic component with a strong similarity between the spatial patterns of historical ENSO-driven extreme precipitation variation (Fig. 4c, Figs. S3c and S4c) and the dynamic component (Figs. 7c,f,i).

Extreme weather often results from ENSO-induced anomalous atmospheric circulation. It has been suggested that with global warming, changes in background SSTs and ENSO related SST patterns may shift atmospheric convection in the tropical Pacific, influence the Walker circulation and alter atmospheric circulation teleconnections, resulting in dynamically induced changes in the intensity of extreme precipitation under future ENSO conditions (Hu et al. 2021; Huang and Xie 2015) in many regions. At the same time, positive feedback due to the latent heating release as moisture condenses can induce stronger large-scale ascent and further enhance extreme precipitation (Nie et al. 2018; Tandon et al. 2018). Both factors affect vertical velocities that correspond to the occurrence of extreme precipitation events. Figure 8 therefore shows the ENSO related circulation variation as indicated by 500-hPa vertical velocity that corresponds to the occurrence of extreme precipitation in historical and future periods. In the historical

Brought to you by UNIVERSITY OF VICTORIA | Unauthenticated | Downloaded 03/18/25 10:15 PM UTC

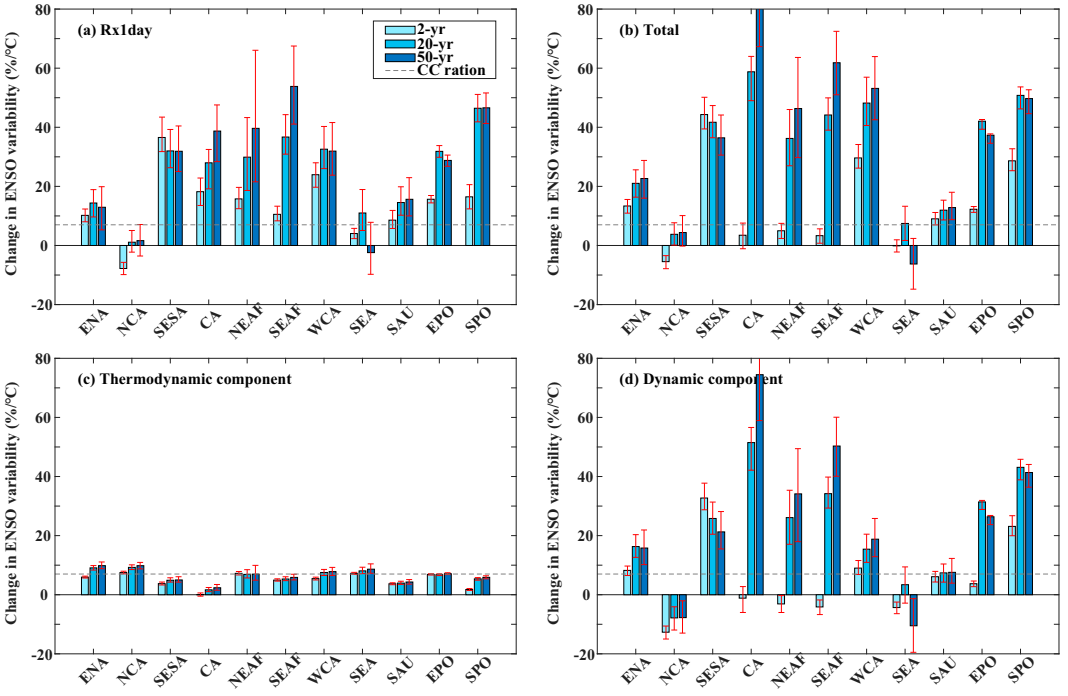

FIG. 6. (a) Changes in future ENSO-driven extreme precipitation variation relative to the period 1950–99. (b) Total component scaling, (c) thermodynamic component scaling, and (d) dynamic component scaling for changes in future ENSO-driven extreme precipitation variation averaged in different regions. Each term is normalized by the historical ENSO-driven extreme precipitation variation and expressed relative to global mean temperatures change in % $°C^{-1}$. Results are presented for extreme precipitation with different intensities, including 2-yr (blue), 20-yr (green), and 50-yr (red) events. The red error bars indicate the 95% uncertainty range estimated by the bootstrapping approach.

period, compared to neutral years, ascending motion in El Niño years enhances moisture convergence in tropical ocean areas, southern North America, west and central Asia, and southeastern South America, which corresponds to the positive El Niño deviation shown in Fig. 4. Correspondingly, descending motion suppresses convergence, resulting in less precipitation, such as in Australia (Figs. 7 and 4). Thus, the patterns of historical ENSO circulation variation correspond strongly to the spatial patterns of historical ENSO-driven extreme precipitation variation for all intensities of extreme precipitation considered.

In the future state, both El Niño and La Niño driven deviation of 500-hPa vertical velocity intensifies over most locations in the ENA, SESA, WCA, EPO, and SPO. This indicates stronger rising motion in future El Niño years and reduced rising motion in future La Niña years, and corresponds to increased ENSO-driven extreme precipitation variation in these regions (Figs. 8g,h). The opposite occurs in SAU, with stronger rising motion in La Niña years and reduced rising motion in El Niño years, again corresponding to increased ENSO-driven extreme precipitation variation (Fig. 8). Furthermore, the dynamic influence on extreme precipitation increases with rarity of those events in some regions, contribution of dynamic components in 20- and 50-yr events are larger than that in 2-yr events. There are regions, however, such as SEA and NCA, where dynamic influences suppress the influence of the mean-state moisture increases and may even result in reduction in extreme precipitation. These are evidently regions where large-scale ENSO related circulation changes that increase local descending motions dominate any change in vertical velocity from local latent heat release. Overall, changes in ENSO circulation exhibit complex spatial variation and are strongly associated with the frequency and intensity of extreme precipitations under different ENSO conditions in the warmer climate state.

6. Discussion

Results based on CESM2 large-ensemble simulations project that extreme precipitation during the boral cold season will generally increase across all ENSO phases in a warmer climate state. Moreover, the influence of ENSO on extreme precipitation variation will strengthen further over most regions that are strongly affected by ENSO. These result in "more extreme and more variable hydroclimate extremes." Our results for wettest events are largely consistent with previous studies for mean precipitation, which project increases in November–April or DJF average precipitation throughout the ENSO cycle as well as intensification of ENSO-driven precipitation variation in the tropical Pacific (Power et al. 2013; Chung and Power 2016) and some land regions, such as eastern North America, western central Asia, southeastern South America, and southern Australia (Sun et al. 2020; Power and Delage 2018) in CMIP3 and CMIP5 coupled models.

Brought to you by UNIVERSITY OF VICTORIA | Unauthenticated | Downloaded 03/18/25 10:15 PM UTC

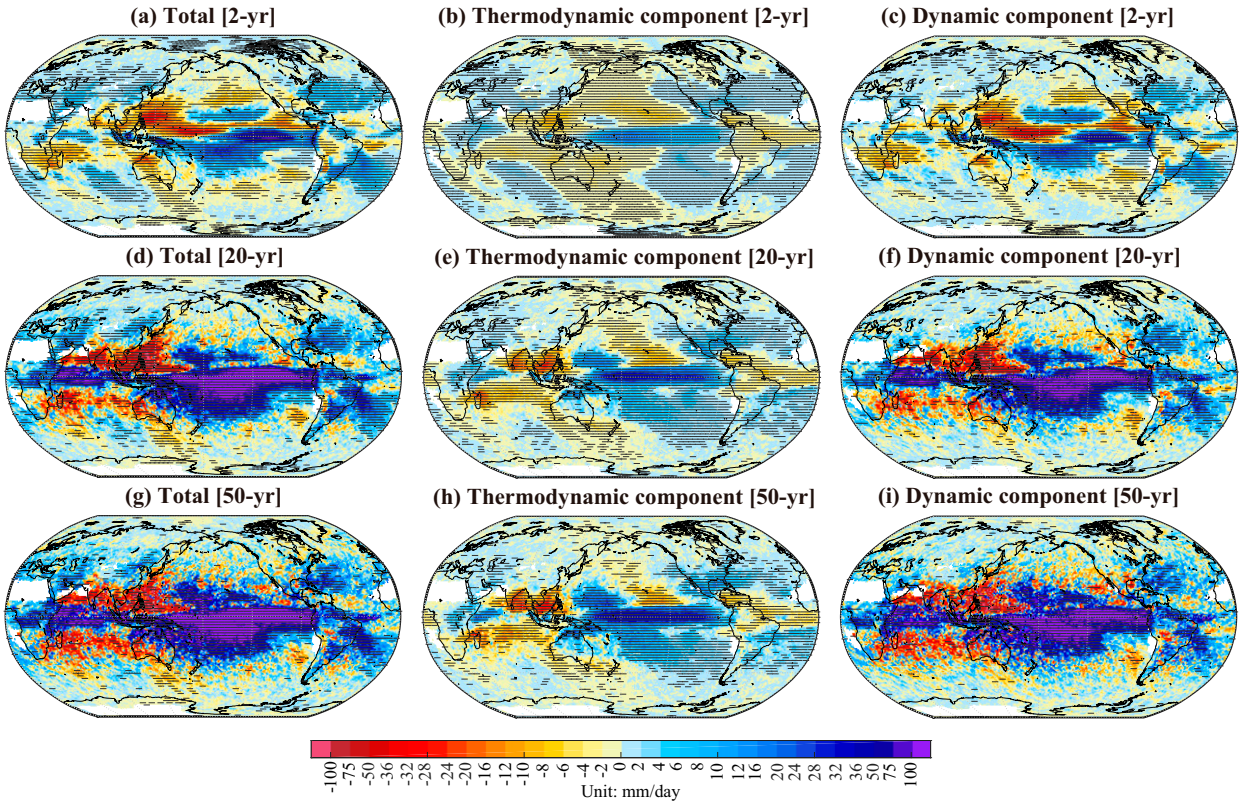

FIG. 7. Physically based diagnostics of thermodynamic and dynamic contributions to changes in ENSO-driven extreme precipitation variation with different intensity levels. Panels show the (a),(d),(g) diagnosed total, (b),(e),(h) thermodynamic, and (c),(f),(i) dynamic components for (a)–(c) 2-, (d)–(f) 20-, and (g)–(i) 50-yr events. Hatching indicates changes that are significantly different from zero at the 5% level.

Some caveats do remain. A potential limitation is that our analysis is primarily based on CESM2. We use this model because it performs better than other models in reproducing observed ENSO characteristics and its teleconnections with extreme precipitation, but this does not necessarily guarantee the robustness of its projections under future emissions scenarios. While less skillful, we therefore also analyzed the CanESM5 and ACCESS-ESM-5 Large Ensemble simulation to evaluate the robustness of our findings to model uncertainties (Figs. S9–S12). Overall, the CanESM5 large ensemble shows some similarity to CESM2 in the direction of changes in El Niño– and La Niña–driven deviations, and in ENSO-driven variation of DJF maximum precipitation events, both globally and in some regions, such as some locations over the ENA, WCA, SAU, and EPO (Fig. S9). In these regions, CanESM5 also shows increases in ENSO-driven extreme precipitation and the likelihood of extreme precipitation under future ENSO phases, with increases in neutral state extreme precipitation and strengthening of the El Niño– and La Niña–driven deviations (Fig. S9). The ACCESS-ESM-5 Large Ensemble, which is the least skillful of the three models in reproducing observed teleconnection relationships with extreme precipitation and the SST-to-Taux coupling, deviates substantially from CESM2 and CanESM5 in its projections of changes in El Niño– and La Niña–driven deviation, and ENSO-driven variation of DJF maximum precipitation events (Fig. S10). In common with CESM2 and CanEM5, it does shows increases in the mean state of extreme precipitation and increases in the likelihood of extreme precipitation under future ENSO phases (Fig. S11). Confidence in its projections is necessarily lower, however, given its lower level of historical skill.

Second, we only use the SST anomaly over the Niño-3.4 region to identify ENSO conditions in both historical and future periods to assess changes in extreme precipitation as well as related changes in circulation and moisture. As noted previously, the overall pattern of SST warming, and the spatial structure of ENSO-related SST variations can affect how the tropical overturning circulations and teleconnection patterns change with warming, which in turn may result in changes in ENSO-driven extreme precipitation variation. Further study will be required to quantify the effect of large-scale circulation change and separate it from the local feedbacks associated with latent heat release and the reduced rising motion that results.

Third, we focus on the wettest 1-day event during the boreal cold season and its changes in variability related to ENSO. The CESM2 offers advances in the surface boundary layer representation for the ocean as well as for cloud microphysics relative to the previous version of the model, CESM1-LE. Nevertheless, CESM2 (and also other CMIP6 models) have fundamental limitations on how well they can simulate

Brought to you by UNIVERSITY OF VICTORIA | Unauthenticated | Downloaded 03/18/25 10:15 PM UTC

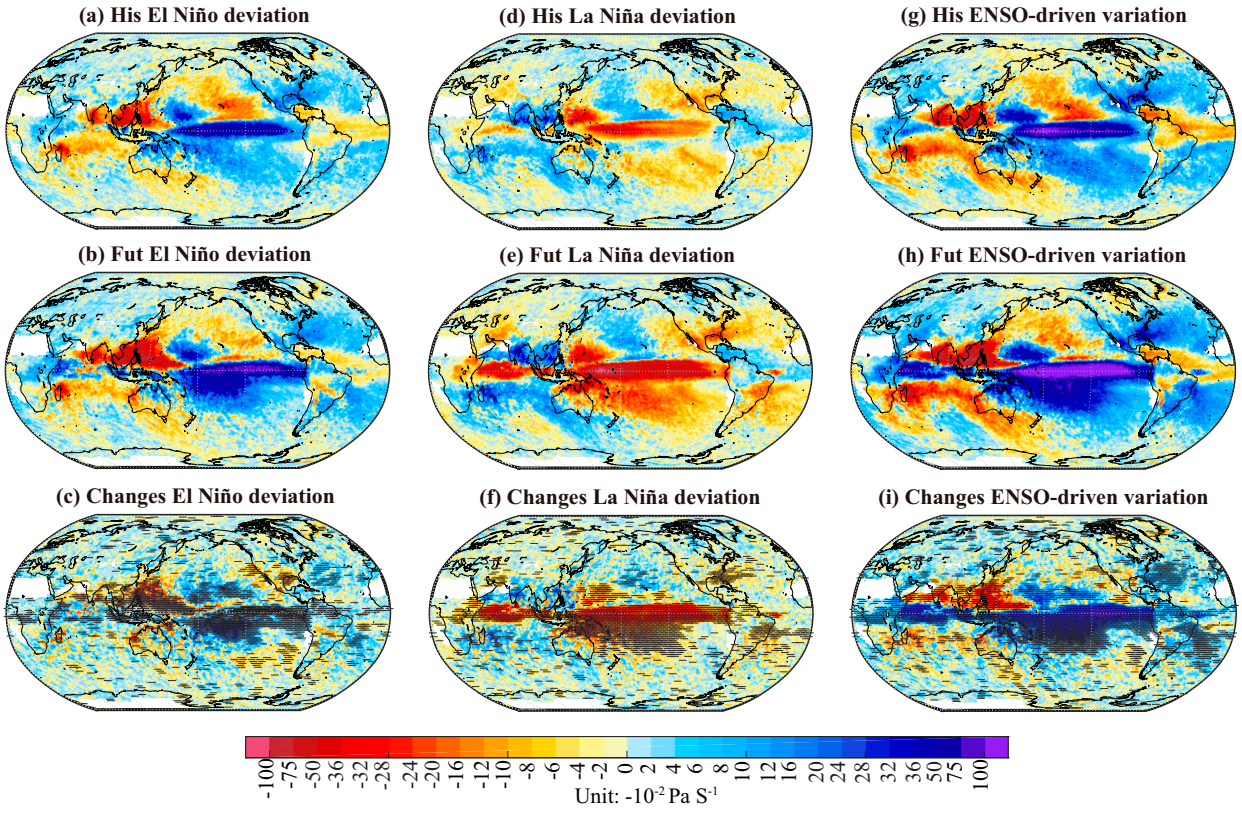

FIG. 8. Spatial patterns of (a)–(c) El Niño–driven deviation, (d)–(f) La Niña–driven deviation, and (g)–(i) ENSO-driven variation of 500-hPa vertical velocity (w) in historical (1950–99) and future (2050–99) periods as well as their differences in the CESM2 large ensemble, all for 20-yr events. Vertical velocity is expressed using pressure as the vertical coordinate. Hatching in (c), (f), and (i) indicates changes that are significantly different from zero at the 5% level.

such extreme events and large-scale teleconnections, in part because they are not able to explicitly represent the vertical transport of energy and water due to atmospheric convection, internal cloud processes, and orographic drag (Hohenegger et al. 2023; Rodgers et al. 2021). However, robust changes in the extreme precipitation and seasonal average precipitation response in coupled models with large-ensemble simulations highlight the usefulness of GCMs in studying how precipitation patterns may change in the future.

7. Conclusions

The evidence that ENSO can alter the intensity and likelihood of damaging extreme precipitation events is clear. Here, we show how these relationships may change in the future under continued greenhouse gas forcing using a model, the new-generation CESM2, which simulates ENSO well under recent, historical, climate forcing conditions. We estimate projected changes in the intensity and probability of extreme precipitation conditional on different ENSO phases and quantify projected changes in ENSO-driven extreme precipitation variation, which measures the difference between the intensity of extreme precipitation under El Niño and La Niña conditions. We also explored the mechanisms that drive changes in extreme precipitation via their decomposition into thermodynamic and dynamic components and considered how the impacts of external forcing manifest themselves regionally. We minimized the uncertainty that arises from unforced internal variability by basing our analysis on a large 50-member initial conditions ensemble.

We found that future warming will intensify the extreme precipitation in all of the regions we considered across all ENSO phases and that differences in the intensity of extreme precipitation under El Niño and La Niña conditions will increase substantially in the future. These changes are the result of a combination of thermodynamic and dynamic responses to external forcing. In most regions, the thermodynamic component alone would result in a relatively uniform intensification of ENSO-driven extreme precipitation variation due to increased total precipitable water caused by surface warming, following the Clausius–Clapeyron relationship. Consistent with this, in most regions, it is projected that there will be an intensification of extreme precipitation in all ENSO phases in future, and that unprecedented extreme events beyond those experienced historically may occur.

The future magnitude of extreme precipitation and its dependence on ENSO phase are heavily influenced by spatially complex dynamical changes as indicated by the dynamical

Brought to you by UNIVERSITY OF VICTORIA | Unauthenticated | Downloaded 03/18/25 10:15 PM UTC

component of our decomposition. These dynamical changes result from both local feedback processes, whereby enhanced precipitation corresponds to increased latent heat release, and thus increased upward motion and moisture convergence, and large-scale ENSO-related circulation changes. In some regions, the dynamical component amplifies the thermodynamic-induced changes, while in others, it offsets them or even result in reduction in extreme precipitation variation.

Dynamical influence is projected to intensify ENSO-driven extreme precipitation variations strongly in some regions, resulting in "more extreme and more variable hydroclimate extremes." In particular, the dynamic component complements the thermodynamic component in the tropical Pacific Ocean and midlatitude regions, such as southeastern South America, western central Asia, and southern Australia. Unprecedented extreme precipitation would occur in southeastern South America, western central Asia, and the equatorial Pacific Ocean during future El Niño years, as well as in southern Australia during future La Niña years, as results of the combined influences of the increased total precipitable water and the stronger reduced rising motions. In addition, the influence of the dynamic component was found to depend on the rarity of extreme events in some regions, with a more important role as precipitation intensity increases. In contrast to the regions mentioned above, ENSO-driven extreme precipitation variations are projected to weaken in northern Central America and Southeast Asia since stronger reduced rising motion in these regions cancels out the influence of the mean-state moisture increases.

Acknowledgments. The study was supported by "Jiangsu Specially-Appointed Professors Program" (1311022201003), the Startup Foundation for Introducing Talent of NUIST (Grant 1523142301195), and the Pan-Canadian Global Water Futures (GWF) research program. We acknowledge the modeling group for producing the CESM2, CanESM5, and ACCESS-ESM-5 Large Ensemble, and the multiple funding agencies who support CMIP6 and ESGF.

Data availability statement. The model output of three CMIP6 models and the ERA5, NCEP1, JRA55, and MERRA datasets are publicly available. ERSSTv5 SST data are available from https://psl.noaa.gov/data/gridded/data.noaa.ersst.v5.html. The HadEX3 data are obtained from https://www.metoffice.gov.uk/hadobs/hadex3/.

REFERENCES

Bonfils, C. J. W., B. D. Santer, T. J. Phillips, K. Marvel, L. R. Leung, C. Doutriaux, and A. Capotondi, 2015: Relative contributions of mean-state shifts and ENSO-driven variability to precipitation changes in a warming climate. *J. Climate*, **28**, 9997–10 013, https://doi.org/10.1175/JCLI-D-15-0341.1.

Cai, W., and Coauthors, 2015: ENSO and greenhouse warming. *Nat. Climate Change*, **5**, 849–859, https://doi.org/10.1038/nclimate2743.

Chung, C. T., and S. B. Power, 2016: Modelled impact of global warming on ENSO-driven precipitation changes in the tropical Pacific. *Climate Dyn.*, **47**, 1303–1323, https://doi.org/10.1007/s00382-015-2902-9.

Donat, M. G., and Coauthors, 2014: Changes in extreme temperature and precipitation in the Arab region: Long-term trends and variability related to ENSO and NAO. *Int. J. Climatol.*, **34**, 581–592, https://doi.org/10.1002/joc.3707.

Dunn, R. J. H., and Coauthors, 2020: Development of an updated global land in situ-based data set of temperature and precipitation extremes: HadEX3. *J. Geophys. Res. Atmos.*, **125**, e2019JD032263, https://doi.org/10.1029/2019JD032263.

Ebita, A., and Coauthors, 2011: The Japanese 55-year reanalysis "JRA-55": An interim report. *SOLA*, **7**, 149–152, https://doi.org/10.2151/sola.2011-038.

Eyring, V., S. Bony, G. A. Meehl, C. A. Senior, B. Stevens, R. J. Stouffer, and K. E. Taylor, 2016: Overview of the coupled model Intercomparison Project Phase 6 (CMIP6) experimental design and organization. *Geosci. Model Dev.*, **9**, 1937–1958, https://doi.org/10.5194/gmd-9-1937-2016.

Grimm, A. M., and R. G. Tedeschi, 2009: ENSO and extreme rainfall events in South America. *J. Climate*, **22**, 1589–1609, https://doi.org/10.1175/2008JCLI2429.1.

Hersbach, H., and Coauthors, 2020: The ERA5 global reanalysis. *Quart. J. Roy. Meteor. Soc.*, **146**, 1999–2049, https://doi.org/10.1002/qj.3803.

Hohenegger, C., and Coauthors, 2023: ICON-Sapphire: Simulating the components of the Earth system and their interactions at kilometer and subkilometer scales. *Geosci. Model Dev.*, **16**, 779–811, https://doi.org/10.5194/gmd-16-779-2023.

Hu, K., G. Huang, P. Huang, Y. Kosaka, and S.-P. Xie, 2021: Intensification of El Niño-induced atmospheric anomalies under greenhouse warming. *Nat. Geosci.*, **14**, 377–382, https://doi.org/10.1038/s41561-021-00730-3.

Huang, B., and Coauthors, 2017: Extended Reconstructed Sea Surface Temperature, version 5 (ERSSTv5): Upgrades, validations, and intercomparisons. *J. Climate*, **30**, 8179–8205, https://doi.org/10.1175/JCLI-D-16-0836.1.

Huang, P., and S.-P. Xie, 2015: Mechanisms of change in ENSO-induced tropical Pacific rainfall variability in a warming climate. *Nat. Geosci.*, **8**, 922–926, https://doi.org/10.1038/ngeo2571.

Iturbide, M., and Coauthors, 2020: An update of IPCC climate reference regions for subcontinental analysis of climate model data: Definition and aggregated datasets. *Earth Syst. Sci. Data*, **12**, 2959–2970, https://doi.org/10.5194/essd-12-2959-2020.

Kalnay, E., and Coauthors, 1996: The NCEP/NCAR 40-Year Reanalysis Project. *Bull. Amer. Meteor. Soc.*, **77**, 437–472, https://doi.org/10.1175/1520-0477(1996)077<0437:TNYRP>2.0.CO;2.

Kenyon, J., and G. C. Hegerl, 2010: Influence of modes of climate variability on global precipitation extremes. *J. Climate*, **23**, 6248–6262, https://doi.org/10.1175/2010JCLI3617.1.

King, A. D., L. V. Alexander, and M. G. Donat, 2013: Asymmetry in the response of eastern Australia extreme rainfall to low-frequency Pacific variability. *Geophys. Res. Lett.*, **40**, 2271–2277, https://doi.org/10.1002/grl.50427.

Klein, S. A., B. J. Soden, and N.-C. Lau, 1999: Remote sea surface temperature variations during ENSO: Evidence for a tropical atmospheric bridge. *J. Climate*, **12**, 917–932, https://doi.org/10.1175/1520-0442(1999)012<0917:RSSTVD>2.0.CO;2.

Kurniadi, A., E. Weller, S.-K. Min, and M.-G. Seong, 2021: Independent ENSO and IOD impacts on rainfall extremes over Indonesia. *Int. J. Climatol.*, **41**, 3640–3656, https://doi.org/10.1002/joc.7040.

Lee, J.-Y., and Coauthors, 2021: Future global climate: Scenario-based projections and near term information. *Climate Change*

Brought to you by UNIVERSITY OF VICTORIA | Unauthenticated | Downloaded 03/18/25 10:15 PM UTC

2021: The Physical Science Basis, V. Masson-Delmotte et al., Eds., Cambridge University Press, 553–672, https://doi.org/10.1017/9781009157896.006.

Li, C., and Coauthors, 2019: Larger increases in more extreme local precipitation events as climate warms. *Geophys. Res. Lett.*, **46**, 6885–6891, https://doi.org/10.1029/2019GL082908.

——, F. Zwiers, X. Zhang, G. Li, Y. Sun, and M. Wehner, 2021: Changes in annual extremes of daily temperature and precipitation in CMIP6 models. *J. Climate*, **34**, 3441–3460, https://doi.org/10.1175/JCLI-D-19-1013.1.

Nie, J., A. H. Sobel, D. A. Shaevitz, and S. Wang, 2018: Dynamic amplification of extreme precipitation sensitivity. *Proc. Natl. Acad. Sci. USA*, **115**, 9467–9472, https://doi.org/10.1073/pnas.1800357115.

O'Neill, B. C., and Coauthors, 2016: The Scenario Model Intercomparison Project (ScenarioMIP) for CMIP6. *Geosci. Model Dev.*, **9**, 3461–3482, https://doi.org/10.5194/gmd-9-3461-2016.

Pendergrass, A. G., and Coauthors, 2017: Precipitation variability increases in a warmer climate. *Sci. Rep.*, **7**, 17966, https://doi.org/10.1038/s41598-017-17966-y.

Pfahl, S., P. A. O'Gorman, and E. M. Fischer, 2017: Understanding the regional pattern of projected future changes in extreme precipitation. *Nat. Climate Change*, **7**, 423–427, https://doi.org/10.1038/nclimate3287.

Planton, Y. Y., and Coauthors, 2021: Evaluating climate models with the CLIVAR 2020 ENSO metrics package. *Bull. Amer. Meteor. Soc.*, **102**, E193–E217, https://doi.org/10.1175/BAMS-D-19-0337.1.

Power, S. B., and F. P. D. Delage, 2018: The El Niño–Southern Oscillation and associated climatic conditions around the world during the latter half of the twenty-first century. *J. Climate*, **31**, 6189–6207, https://doi.org/10.1175/JCLI-D-18-0138.1.

——, ——, C. Chung, G. Kociuba, and K. Keay, 2013: Robust twenty-first-century projections of El Niño and related precipitation variability. *Nature*, **502**, 541–545, https://doi.org/10.1038/nature12580.

Rienecker, M. M., and Coauthors, 2011: MERRA: NASA's modern-era retrospective analysis for research and applications. *J. Climate*, **24**, 3624–3648, https://doi.org/10.1175/JCLI-D-11-00015.1.

Rind, D., R. Goldberg, and R. Ruedy, 1989: Change in climate variability in the 21st century. *Climatic Change*, **14**, 5–37, https://doi.org/10.1007/BF00140173.

Rodgers, K. B., and Coauthors, 2021: Ubiquity of human-induced changes in climate variability. *Earth Syst. Dyn.*, **12**, 1393–1411, https://doi.org/10.5194/esd-12-1393-2021.

Schubert, S. D., Y. Chang, M. J. Suarez, and P. J. Pegion, 2008: ENSO and wintertime extreme precipitation events over the contiguous United States. *J. Climate*, **21**, 22–39, https://doi.org/10.1175/2007JCLI1705.1.

Shang, H., J. Yan, and X. Zhang, 2011: El Niño–Southern Oscillation influence on winter maximum daily precipitation in California in a spatial model. *Water Resour. Res.*, **47**, W11507, https://doi.org/10.1029/2011WR010415.

Singh, J., M. Ashfaq, C. B. Skinner, W. B. Anderson, V. Mishra, and D. Singh, 2022: Enhanced risk of concurrent regional droughts with increased ENSO variability and warming. *Nat. Climate Change*, **12**, 163–170, https://doi.org/10.1038/s41558-021-01276-3.

Sun, Q., C. Miao, A. AghaKouchak, I. Mallakpour, D. Ji, and Q. Duan, 2020: Possible increased frequency of ENSO-related dry and wet conditions over some major watersheds in a warming climate. *Bull. Amer. Meteor. Soc.*, **101**, E409–E426, https://doi.org/10.1175/BAMS-D-18-0258.1.

——, X. Zhang, F. Zwiers, S. Westra, and L. V. Alexander, 2021: A global, continental, and regional analysis of changes in extreme precipitation. *J. Climate*, **34**, 243–258, https://doi.org/10.1175/JCLI-D-19-0892.1.

Supari, F. Tangang, E. Salimun, E. Aldrian, A. Sopaheluwakan, and L. Juneng, 2018: ENSO modulation of seasonal rainfall and extremes in Indonesia. *Climate Dyn.*, **51**, 2559–2580, https://doi.org/10.1007/s00382-017-4028-8.

Tandon, N. F., X. Zhang, and A. H. Sobel, 2018: Understanding the dynamics of future changes in extreme precipitation intensity. *Geophys. Res. Lett.*, **45**, 2870–2878, https://doi.org/10.1002/2017GL076361.

Taylor, R. G., M. C. Todd, L. Kongola, L. Maurice, E. Nahozya, H. Sanga, and A. M. MacDonald, 2013: Evidence of the dependence of groundwater resources on extreme rainfall in East Africa. *Nat. Climate Change*, **3**, 374–378, https://doi.org/10.1038/nclimate1731.

Uppala, S., 2007: Use of satellite data in reanalyses. ECMWF, 22 pp., https://www.ecmwf.int/sites/default/files/elibrary/2008/12887-use-satellite-data-reanalyses.pdf.

Yang, Y.-M., J.-H. Park, S.-Il. An, B. Wang, and X. Luo, 2021: Mean sea surface temperature changes influence ENSO-related precipitation changes in the mid-latitudes. *Nat. Commun.*, **12**, 1495, https://doi.org/10.1038/s41467-021-21787-z.

Zhang, X., J. Wang, F. W. Zwiers, and P. Y. Groisman, 2010: The influence of large-scale climate variability on winter maximum daily precipitation over North America. *J. Climate*, **23**, 2902–2915, https://doi.org/10.1175/2010JCLI3249.1.

Brought to you by UNIVERSITY OF VICTORIA | Unauthenticated | Downloaded 03/18/25 10:15 PM UTC